Vp and Vs structure estimations from ambient seafloor noise observed by distributed acoustic sensing

T. Tonegawa[1], E. Araki[1], H. Matsumoto[1], T. Kimura[1], K. Obana[1], G. Fujie[1], R. Arai[1], K. Shiraishi[1], M. Nakano[1], Y. Nakamura[1], T. Yokobiki[1], and S. Kodaira[1]

[1] Japan Agency for Marine-Earth Science and Technology (JAMSTEC), 2-15, Natsushima, Yokosuka Kanagawa, 237-0061, Japan.

Corresponding author: Takashi Tonegawa (tonegawa@jamstec.go.jp)

Key Points:

- We estimated the shallow *Vp* and *Vs* structures below a submarine cable in the Nankai subduction zone, Japan.
- *P* waves were extracted from ambient noise records observed by DAS using *f-k* filtering.
- The extraction of *P* waves depends on weather conditions, and can be perfomed on stormy days.

Abstract

Seismic velocity structures have been estimated using ambient noise records observed by distributed acoustic sensing (DAS) technology. Previous studies have obtained *S*-wave velocity (*Vs*) structures along submarine cables using surface waves; however *P*-wave velocity (*Vp*) structure have seldom been constructed because ambient noise primarily contains surface waves. Here, we show *P* and Rayleigh wave extractions from ambient seafloor noise observed by DAS, and also estimate the *Vp* and *Vs* structures along a submarine cable deployed off Cape Muroto in the Nankai subduction zone, Japan. To extract the *P* waves, we calculated the cross-correlation functions (CCFs) of the ambient noise and applied a frequency-wavenumber filter to the CCFs to remove the effects of slower surface waves. The results indicate that similar features can be obtained in the *Vp* and *Vs* profiles, and that the *P* wave extractions can be performed on days with poor weather conditions.

Plain Language Summary

The density of seismic observations on land is typically higher than those in the ocean. However, higher density observations in both land and ocean regions can be made using the recently developed distributed acoustic sensing (DAS). DAS is capable of measuring the wavefields of earthquakes and other natural phenomena in detail. The densely sampled wavefields by DAS are also useful for investigating seismic velocity structures underneath cables Previous studies have estimated *S*-wave velocity structures using ambient noise records from submarine cables. Although methods for estimating *P*-wave velocity structures have not been established in previous DAS studies, we successfully retrieved *P* waves from the ambient noise using frequency-wavenumber filtering. We then applied the retrieved waves to estimate shallow *P*-wave velocity profiles below a submarine cable in the Nankai subduction zone, southwest of Japan. Because *P* and *S* wave velocities have different sensitivities to fluids in subseafloor structures, estimating the physical properties aids our understanding of the detailed structure and thereby makes the monitoring of the structure with high resolutions in space more effective.

1 Introduction

Distributed acoustic sensing (DAS) using fiber optic cables is now a powerful tool for detecting signals of various wave propagations, because the station density along a cable is higher than the typical density of seismic observations using individual seismic sensors. For example, DAS on land is capable of observing signals from regional (Lindsey et al. 2017) and teleseismic earthquakes (Yu et al. 2019) and can estimate shallow *S*-wave velocity (*Vs*) structure from ambient noise records (Dou et al. 2017; Ajo-Franklin et al. 2019). DAS in submarine cables can capture seismic waves from earthquakes (Sladen et al. 2019; Lindsey et al. 2020; Lior et al. 2021) and also ocean-specific wavefields, including infragravity waves (Williams et al. 2019) and hydroacoustic waves (Matsumoto et al. 2021).

As with land cases, ambient noise records observed by DAS have recently been used to estimate the seismic velocity structures beneath submarine cables. Previous studies have estimated the *Vs* structures within sediment layers in the Japan Trench (Spica et al. 2020) and in the Monterey Bay, California (Cheng et al. 2021). However, *P*-wave velocity (*Vp*) structures have not been estimated using ambient noise observed by DAS. This is likely because DAS-

based ambient noise records are dominated by surface waves related to microseisms. However, wave-wave interactions from ocean swells indeed excite *P* waves (Longuet-Higgins, 1950; Hasselmann, 1963), as they can be observed in global (Gerstoft et al., 2006; Landès et al., 2010; Farra et al., 2016; Gualtieri et al., 2014; Koper et al., 2010; Nishida and Takagi, 2016) and local (Tonegawa et al. 2021) seismic observations. This means that ambient noise acquired by DAS potentially contain *P* waves that were excited at local scales.

In this study, ambient noise records observed by a submarine cable deployed off Cape Muroto in the Nankai subduction zone, Japan (Fig. 1) are employed to extract *P* and surface waves. We hereafter refer to the cable as the Muroto cable. Using the retrieved wavefields, we estimate the *Vp* and *Vs* structures beneath the Muroto cable. The Philippine Sea Plate subducts northwards in the Nankai Trough (Fig. 1), and the accretionary prism is located north of the trough. The Muroto cable was deployed on the soft sediment of the accretionary prism, and ambient noise records observed by the cable are plausibly dominated by surface waves propagating within the prism. We therefore apply a frequency-wavenumber (*f*-*k*) filter to remove the effects of slowly-propagating surface waves. Such an approach can be accomplished with the densely sampled seismic traces acquired by DAS.

2 Data

The Muroto cable is 128 km long (Fig. 1), of which the cable section from 0.35 km to 2.14 km is buried 0.5-1.0 m beneath the seafloor, but the rest of the cable seawards is unburied and lays on the seafloor with its own weight (Matsumoto et al. 2021). The DAS data was observed by AP Sensing (model N5200A) over a sensing length of 50 km along the cable, with a gauge length of 40.4 m and a sensor spacing of 5.1 m, in which a 16-bit recording of the differential strain (strain rate) at each channel was measured by the interrogator. Detailed descriptions of the cable and AP Sensing observations can be found in Matsumoto et al. (2021) and Ide et al. (2021), respectively. The water depth of the cable ranges between 0 and 1,100 m, and topographic relief is present at a cable distance of 30 km from the coastline. The relief continues eastwards to a shallow bank called Tosa-Bae, beneath which a large seamount is

subducting (Kodaira et al. 2002). The sampling rate was decimated from 500 Hz to 50 Hz for the processing in this study. The observation period was January 27–31, 2021.

Fig. 1

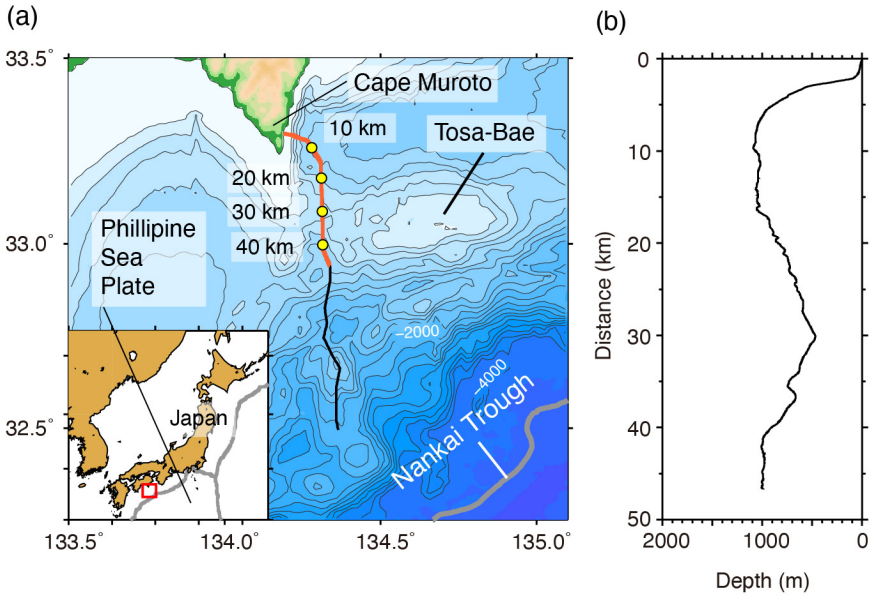

Figure 1. Geometry of the Muroto cable on the seafloor. (a) Black and red lines show the location of the Muroto cable and the section used for the DAS measurements with 10 km increments (yellow circles), respectively. (b) Water depths along the Muroto cable.

3 Methods

3.1 Ambient noise analysis

The space sampling of 5.1 m on the continuous records was decimated to 51 m by stacking the records within a spacing of –20.5~25.5 m for each 5.1-m station. We divided the cable into 17 subarrays with reference point increments of 2.5 km, wherein each subarray that has a separation distance of 5 km from the reference point to the farthest station was secured: Stations at the cable distances more than 5 km from the reference points are secured in the subarrays because the cable is not linear. The reference points along the cable are summarized in Table S1. Within each subarray, using the continuous records with a time window of 75 s, cross-correlation functions (CCFs) were calculated using the spectral whitening in the frequency domain (Bensen 2007; Brenguier 2007). The CCFs for all station pairs in each subarray were stacked using a 50 m spatial bin and over one day in time. Fig. 2(a) shows that the obtained

wavefield at a frequency of 0.4–0.8 Hz is the fundamental mode of a Rayleigh wave with a propagation velocity of < 1.0 km/s.

Fig. 2

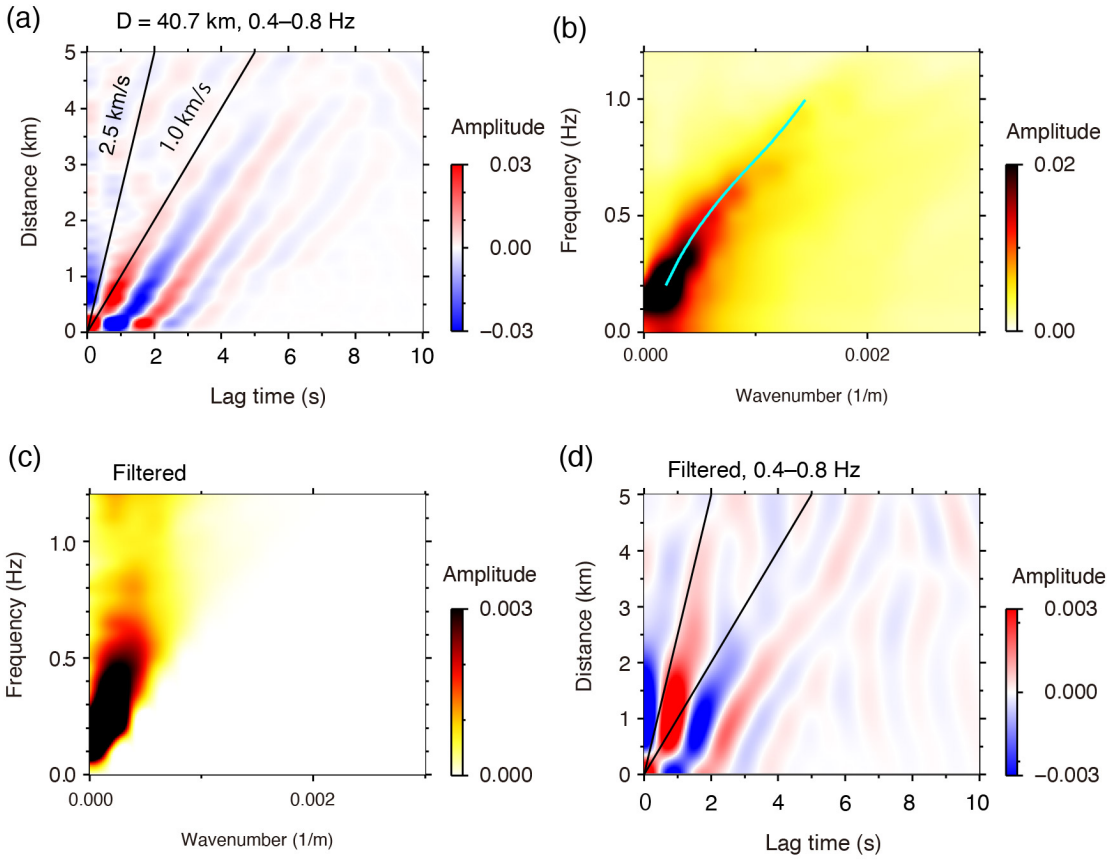

Figure 2. Cross-correlation functions (CCFs) s in the time-distance and *f-k* domains for subarray 16 (cable reference point D = 40.7 km) on January 27, 2020. (a) CCFs at 0.4–0.8 Hz aligned as a function of the separation distance between two stations. The two lines show the reference propagation velocities of 1.0 and 2.5 km/s. (b) CCFs in the *f-k* domain with (light-blue line) the picked dispersion curve (c) CCFs in the *f-k* domain after applying the Eq. (1) filter to those in Fig. 2b. (d) CCFs in the time-distance domain with the *f-k* filter of Eq. (1).

3.2 FK analysis of surface and P waves

We applied the Fourier transform to the one-day CCF dataset from each subarray to obtain the CCFs in the *f-k* domain (Fig. 2b). To obtain the dispersion curve of the Rayleigh wave, the maximum amplitude at each frequency between 0.2 and 1.0 Hz was searched within a phase velocity range of 200–1200 m/s in the *f-k* domain. Here, for some subarrays, because the dispersion curves of higher and lower frequency sides within the frequency range were unstable, we limited the frequency bands at the stations for velocity estimations, which are summarized

126 them in Table S1. Also, since the dispersion curve at a subarray near the coastline could not be
127 determined, we estimated vertical velocity profiles beneath only 16 subarrays.

128 We further applied a Gaussian filter to the CCFs in the *f-k* domain to remove waves with
129 slow propagation velocities, including the Rayleigh wave. The Gaussian filter is described as

130 $$G(f,k) = \exp\left\{-\left(\frac{\pi k}{Af/c}\right)^2\right\} \quad (1),$$

131 where c is a cutoff velocity and A is a constant, referring to Eequation (6) in Wilson & Aster
132 (2005). We set those as c = 1600 m/s and A = 3.5. For example, at a frequency of 0.4 Hz, G
133 results in 0.8790, 0.3134, and 2.523 x 10^{-6} when k = 0.0001, 0.0003, and 0.001. This function
134 suppresses the amplitudes corresponding to waves that are slower than 1600 m/s in the *f-k*
135 domain (Fig. 2c), and also in the time-distance domain (Fig. 2d). Such suppressions can also be
136 observed at other locations along the cable (Fig. S1).

137

138 **3.3 Vs profile estimation**

139 For each subarray, we estimated the one-dimensional (1D) *Vs* model with the dispersion
140 curve of the Rayleigh wave using a non-linear inversion, simulated annealing. Simulated
141 annealing is a Monte Carlo method that searches the global minimum by lowering the possibility
142 of the acceptance of random perturbations to the model parameters with decreasing temperature
143 (e.g. Chevrot 2002). The misfit function is described as

144 $$E = \sum_{i=1}^{M} \left| c_{obs}(f_i) - c_{syn}(f_i) \right| \quad (2),$$

145 where $c_{obs}(f_i)$ and $c_{syn}(f_i)$ are the observed and predicted phase velocities, respectively, for i-th
146 frequency ($i = 1 \cdots M$). The predicted phase velocity was calculated using DISPER80 (Saito
147 1988). A 1D *Vs* model averaged over all the 1D *Vs* models beneath the seafloor obtained for the
148 Nankai subduction zone (Tonegawa et al. 2017) was selected as the initial *Vs* model. The *Vp* and
149 density models were converted from *Vs* using empirical relationships (Brocher, 2005).

150 The update of v_k is based on a previous study (Tonegawa et al. 2017), where v_k is the 1D
151 *Vs* profile at the k-th layer. At each iteration step, we perturbed v_k by a depth interval of 0.1 km
152 using random numbers, referring to a previous study (Chevrot 2002). The updated v_k' is
153 described as

154 $$v_k' = \begin{cases} v_k - \Delta v & if\ \alpha < 0.5 \\ v_k + \Delta v & if\ \alpha > 0.5 \end{cases} \quad (3),$$

155 where α is a random number between 0 and 1. The velocity perturbation is Δv = 0.02 km s^{-1}. The
156 minimum perturbed velocity was set as 0.4 km s^{-1}. Similar to the previous study (Tonegawa et
157 al. 2017), the maximum velocity gradients above and below 2 km beneath the seafloor were set
158 as 2.0 s^{-1} and 1.0 s^{-1}, respectively. The updated v_k' is accepted when $\Delta E \leq 0$, where ΔE is the

difference between E and that of the previous iteration. If $\Delta E \geq 0$, the acceptance depends on the probability,

$$P = \exp\left(-\frac{\Delta E}{T}\right) \quad (4),$$

where T is the temperature. The annealing schedule at the n-th step can be written as $T_n = \gamma^n T_0$, and we set $\gamma = 0.996$ and $T_0 = 3E_0$, where E_0 is the result of the first step of the estimation E. If a random number between 0 and 1, α, is less than P, the updated v_k' is accepted. The Vp and density models are also updated using the empirical relationships after the acceptance of v_k'. In order to estimate the error of the Vs profile at each subarray, we prepared 30 profiles of v_k' with changing random number seeds for the inversion, and estimated the standard deviations from the obtained profiles.

3.4 Vp profile estimation

We estimated the Vp profile for each subarray using the τ-sum inversion method (Diebold & Stoffa, 1981; Stoffa et al. 1981; Shinohara et al. 1994). The CCFs in the distance-time domain (e.g. Fig. 2a and Figs. S1a and e) can be converted to those in the τ-p domain (e.g. Fig. 3) using slant stacking (Stoffa et al. 1981), where p is the slowness and τ is the intercept of the tangent line of the travel time curve to the time axis. The CCFs in a frequency band of 0.4–0.8 Hz were used. The τ-sum inversion using the discretely sampled τ-p data (Fig. 3) can be performed by,

$$\begin{cases} h_1 = \dfrac{\frac{\tau(p_2)}{2}}{(p_1^2 - p_2^2)^{\frac{1}{2}}} \\ h_i = \dfrac{\frac{\tau(p_{i+1})}{2} - \sum_{k-1}^{i-1}(p_k^2 - p_{k+1}^2)^{1/2} h_k}{(p_i^2 - p_{i+1}^2)^{1/2}} \quad i \geq 2 \end{cases} \quad (5),$$

where h is the thickness of a layer with a velocity of $1/p_i$ (Shinohara et al. 1994). The standard deviations of the τ-p data were estimated using a bootstrapping technique with 50 times (Fig. 3), and the error in the Vp profiles were estimated using upper and lower bounds ($\pm 1\sigma$) of the τ-p data. Because it is difficult to precisely describe low velocity layers using this technique,

velocities between the regions above and below a low velocity layer are connected in the inversion and hence low velocity layers are neglected in the *Vp* profiles.

Fig. 3

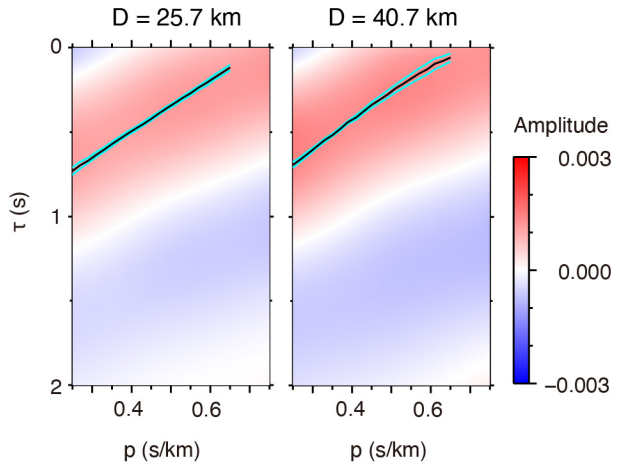

Figure 3. Slant stacking results of the CCFs at 0.4–0.8 Hz for subarrays (left) 10 and (right) 16 on January 27, 2020. Black and light-blue lines indicate the τ-p data and $\pm 1\sigma$ from the bootstrapping technique with 50 times.

4 Results

Figure 4a shows the 1D *Vs* structures for the 16 subarrays along the cable (January 29, 2020), in which the following four features were identified. (1) A shallow high velocity body is present at the northern part of the cable (7–12 km in horizontal distance), which corresponds to the high *Vs* landward structure. (2) From north to south, the high velocity region at the bottom of the profile tends to be shallow and peaked slightly south of the seafloor topographic high. This may be related to the deformation of the accretionary prism due to the subducting seamount. (3) The shallow *Vs* values are relatively high and low in the ridge and basin regions, respectively. (4) Moreover, a high velocity volume can be observed (at ~30 km in horizontal distance) within a shallow slower velocity region. Although the errors of the *Vs* profiles at the bottom are relatively large, these at other regions are sufficiently small (Fig. 4c). Moreover, the features (1), (3) and (4) are enhanced in the *Vs* perturbation profiles (Fig. S2), in which the perturbations were estimated with the reference profile averaged over the 16 *Vs* profiles beneath the seafloor. The feature (2) was diminished when averaging the 16 *Vs* profiles, but a high velocity region located south of the topographic relief was enhanced ((2)' in Fig. S2).

The 1D *Vp* strucrure contained similar features to those observed in the 1D *Vs* profiles (Fig. 4b), including (1) and (2). However, significant velocity changes at shallow depths (3) are not observed. This may be because *Vs* is more sensitive to the amount of water in the marine sediment than *Vp*. In addition, the high velocity volume at 30 km in horizontal distance (4)

cannot be observed. Although the errors of the *Vp* profiles are relatilvey large compared with those of the *Vs* profiles, they are largely less than 0.1 km/s (Fig. 4d).

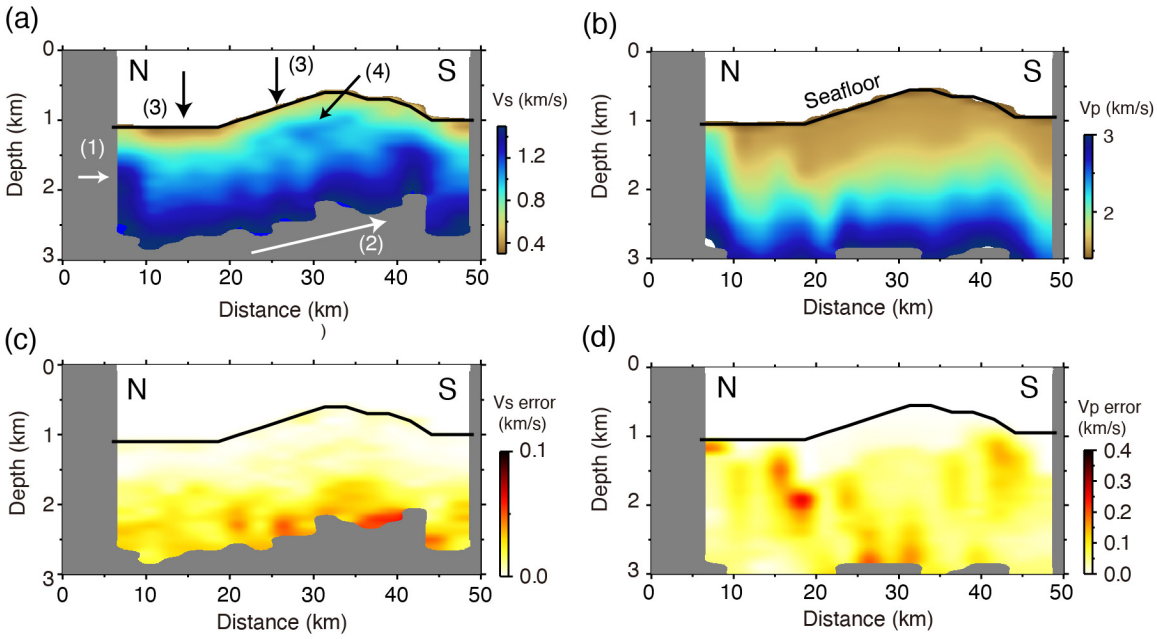

Figure 4. Seismic velocity profiles along the Muroto cable. (a) *Vs* profiles along the cable, created using the CCFs on January 29, 2020. Specific features (1)–(4) are observed (see detailed in the text). (b) *Vp* profiles along the cable, generated using the CCFs on January 27, 2020. (c) Error for panel (a). (d) Error for panel (b).

5 Discussion

5.1 P wave extraction and weather conditions

We only used the ambient noise records from January 27, 2020, for imaging the 1D *Vp* structure, because the *P* wave extractions at some subarrays were failed when using the ambient noise records from the other days in the observation period. Even if *P* waves could be successfully extracted, their amplitudes were smaller. Figure S3 shows the daily *P* wave extractions at 25.7 km and 30.3 km along the cable. The P wave retrievals on January 27 are clear, wheares the *P* waves cannot be extracted at 30.3 km and has smaller amplitudes at 25.7 km o the other three days of the observation period.

We attributed extraction quality to the weather conditions in the observation period. An atmospheric low pressure system passed near Japan on January 27, and it affected the intensity of ocean swell until January 27. The *P* wave extractions in this study were performed at frequencies lower than ~0.8 Hz (Fig. 2c), which are within the typical frequency range of microseisms (e.g., 0.05–2 Hz). Because microseisms are mainly excited by wave-wave interactions associated with ocean swell (Longuet-Higgins 1950; Hasselmann, 1963), the *P* wave retrievals are likely affected by the intensity of the ocean swell. Indeed, the significant wave height observed off Cape

Muroto by a Global Positioning System (GPS) buoy (The Nationwide Ocean Wave information network for Ports and HArbourS (NOWPHAS)) was large on January 27 and 28 (Fig. S4). Therefore, our observations indicate that near-field *P* waves are excited by ocean swell, and that the *P* wave retrievals depend on weather conditions.

The *P* wave extractions are related to the strain of the *P* wavefield observed in the horizontal plane. The ambient noise records observed by DAS almost represent the horizontal component of seafloor motion, which unables us to observe *P* waves with near-vertical incidences to the seafloor. However, we calculated the CCFs by removing the effects of waves slower than 1600 m/s up to a separation distance of 10 km for each subarray. We found that the maximum distance that a *P* wave reaches is roughly ~8–10 km (Fig. S5a-d), which indicates that the raypath of the *P* wave to the seafloor has a larger incidence angle from the vertically downwards than those with greater offsets (Fig. S5e). In this case, observable amplitudes of the *P* wave can be projected onto the horizontal plane, and we consider that our observations retrieved such near-field *P* waves.

5.2 Stability of the obtained velocity profiles

In order to evaluate the stability of the obtained *Vs* profiles, we created profiles for the other 4 days (Fig. S6). The results for these days reproduced the features (1)–(4) shown in Fig. 4b. The standard deviations at the top of the shallow high velocity region at the northern part are relatively large. This is probably because the velocity gradient in this region is large. To obtain a reliable velocity structure in this region, the stacking period of the CCFs may be extended. In contrast, the *Vs* in the other parts were stable and fluctuated less than ~0.06 km/s. Around the relief, the *Vs* fluctuations were less than 0.03 km/s at depths less than 0.5 km below the seafloor. If a large temporal change in *Vs* occurred (due to a large earthquake), it may be possible to monitor its variations at shallow depths.

5.3 Interpretation of Vp and Vs structures

Although the *Vp* profiles did not include the feature (4) or the underlying lower velocities, the obtained *Vs* profiles, which are sensitive to low velocity layers, shows an isolated high velocity volume. Two possibilities are invoked for explaining the presence of this volume. The first is that a high-velocity rock is isolated from the high velocity region at the bottom during the formation of the accretionary prism. The second possibility is that gas-hydrate sediments with a higher velocity are present in this area and overlie a free gas layer with a lower velocity. The observed high velocity body has a *Vs* of 1.1 km/s, which is higher than the surrounding sediment (0.8–0.9 km/s). Because the *Vs* of pure methane hydrate is 1.89 km/s (Waite et al. 2000), the observed high velocity volume can be explained by a fraction of methane hydrate within the sediment. Such gas-hydrate sediments have been detected and explored by identifying bottom simulating reflectors (BSRs) from seismic exploration surveys. Indeed, BSRs have been identified at other locations in the Nankai accretionary prism and occur intermittently due to the deformation of the accretionary prism (e.g., Yamano et al. 1982; Ashi et al. 2002;

Nouzé et al. 2004; Ohde et al. 2018). Since gas-hydrate sediments and a free gas layer may be present in this region, additional investigation, including seismic surveys and sediment cores by drilling, is expected to identify the high velocity body along the Muroto cable.

6 Conclusions

We estimated *Vp* and *Vs* profiles from the CCFs using ambient noise records observed by DAS. In particular, *P* waves could be extracted by removing slower waves with an *f-k* filter. Such filtering can be performed on spatially regular and densely sampled DAS records. However, *P* wave extractions depend on weather conditions and can be accomplished on stormy days. In addition, although the *Vs* profiles obtained using the one-day CCFs were slightly unstable in specific regions, we expect that the subseafloor structures along the Muroto cable, including gas-hydrates, can be monitored if the stacking period and observation periods can be extended.

Acknowledgments, Samples, and Data

We used significant wave height data provided by The Nationwide Ocean Wave information network for Ports and HArbourS (NOWPHAS) (https://www.mlit.go.jp/kowan/nowphas/index_eng.html).

Data Availability Statement

The data that is used for reproducing all the figures are available online (Zenodo: doi:10.5281/zenodo.4876758).

References

Ajo-Franklin, J. B., Dou, S., Lindsey, N. J., Monga, I., Tracy, C., Robertson, M., et al. (2019). Distributed Acoustic Sensing Using Dark Fiber for Near-Surface Characterization and Broadband Seismic Event Detection. *Scientific Reports*, *9*, 1328. http://doi.org/10.1038/s41598-018-36675-8

Ashi, J., Tokuyama, H., & Taira, A. (2002). Distribution of methane hydrate BSRs and its implications for the prism growth in the Nankai Trough. *Marine Geology*, *187*, 177–191.

Bensen, G. D., Ritzwoller, M. H., Barmin, M. P., Levshin, A. L., Lin, F., Moschetti, M. P., et al. (2007). Processing seismic ambient noise data to obtain reliable broad-band surface wave dispersion measurements. *Geophysical Journal International*, *169*(3), 1239–1260. http://doi.org/10.1111/j.1365-246X.2007.03374.x

309 Brenguier, F., Shapiro, N. M., Campillo, M., Nercessian, A., & Ferrazzini, V. (2007). 3-D
310 surface wave tomography of the Piton de la Fournaise volcano using seismic noise
311 correlations. *Geophysical Research Letters*, *34*(2), 1351–5.
312 http://doi.org/10.1029/2006GL028586
313
314 Brocher, T. M. (2005). Empirical Relations between Elastic Wavespeeds and Density in the
315 Earth's Crust. *Bulletin of the Seismological Society of America*, *95*(6), 2081–2092.
316 http://doi.org/10.1785/0120050077
317
318 Cheng, F., Chi, B., Lindsey, N. J., Dawe, T. C., & Ajo-Franklin, J. B. (2021). Utilizing
319 distributed acoustic sensing and ocean bottom fiber optic cables for submarine structural
320 characterization. *Scientific Reports*, *11*, 1–14. http://doi.org/10.1038/s41598-021-84845-y
321
322 Chevrot, S. (2002). Optimal measurement of relative and absolute delay times by simulated
323 annealing. *Geophysical Journal International*, *151*, 164–171.
324
325 Diebold, J. B., & Stoffa, P. L. (1981). The traveltime equation, tau-p mapping, and inversion of
326 common midpoint data, *46*(3), 238–254. http://doi.org/10.1190/1.1441196
327
328 Dou, S., Lindsey, N., Wagner, A. M., Daley, T. M., Freifeld, B., Robertson, M., et al. (2017).
329 Distributed Acoustic Sensing for Seismic Monitoring of The Near Surface: A Traffic-
330 Noise Interferometry Case Study. *Scientific Reports*, *7*, 11620.
331 http://doi.org/10.1038/s41598-017-11986-4
332
333 Farra, V., Stutzmann, E., Gualtieri, L., Schimmel, M., & Ardhuin, F. (2016). Ray-theoretical
334 modeling of secondary microseism Pwaves. *Geophysical Journal International* 206,
335 1730–1739. http:/doi.org/10.1093/gji/ggw242.
336
337 Gerstoft, P., Fehler, M. C., & Sabra, K. G. (2006). When Katrina hit California. *Geophys. Res.*
338 *Lett.* 33, Q04009–6. http://doi.org/10.1029/2006GL027270.
339
340 Gualtieri, L., Stutzmann, E., Farra, V., Capdeville, Y., Schimmel, M., Ardhuin, F., et al. (2014).
341 Modelling the ocean site effect on seismic noise body waves. *Geophysical Journal*
342 *International* 197, 1096–1106. http:/doi.org/10.1093/gji/ggu042.
343
344 Hasselmann, K. (1963). A Statistical Analysis of the Generation of Microseisms. *Review of*
345 *Geophysics* 1, 177–210.
346

Ide, S., Araki, E., & Matsumoto, H. (2021). Very broadband strain-rate measurements along a submarine fiber-optic cable off Cape Muroto, Nankai subduction zone, Japan. *Earth, Planets and Space*, *73*, 1–10. http://doi.org/10.1186/s40623-021-01385-5

Kodaira, S., Kurashimo, E., Park, J.-O., Takahashi, N., Nakanishi, A., Miura, S. et al. (2002). Structural factors controlling the rupture process of a megathrust earthquake at the Nankai trough seismogenic zone, *J. Geophys. Res.*, **149**, 815–835.

Koper, K. D., Seats, K., & Benz, H. (2010). On the Composition of Earth's Short-Period Seismic Noise Field. *Bulletin of the Seismological Society of America* 100, 606–617. http://doi.org/10.1785/0120090120.

Landès, M., Hubans, F., Shapiro, N. M., Paul, A., & Campillo, M. (2010). Origin of deep ocean microseisms by using teleseismic body waves. *J. Geophys. Res.* 115, 672–14. http://doi.org/10.1029/2009JB006918.

Lindsey, N. J., Martin, E. R., Dreger, D. S., Freifeld, B., Cole, S., James, S., et al. (2017). Fiber-Optic Network Observations of Earthquake Wavefields. *Geophysical Research Letters*, *44*, 11792–11799. http://doi.org/10.1002/2017GL075722

Lior, I., Sladen, A., Rivet, D., Ampuero, J.-P., Hello, Y., Lamare, P., et al. (2021). On the Detection Capabilities of Underwater Distributed Acoustic Sensing. *Journal of Geophysical Research*, *126*(3), e2020JB020925. http://doi.org/10.1002/essoar.10504330.1

Longuet-Higgins, M. S. (1950). A THEORY OF THE ORIGIN OF MICROSEISMS. *Philosophical Transactions of the Royal Society of London. Series a, Mathematical and Physical Sciences*, *243*(857), 1–35.

Matsumoto, H., Araki, E., Kimura, T., Fujie, G., Shiraishi, K., Tonegawa, T., et al. (2021). Detection of hydroacoustic signals on a fiber-optic submarine cable, 1–12. http://doi.org/10.1038/s41598-021-82093-8

Nishida, K., & Takagi, R. (2016). Teleseismic S wave microseisms. *Science* 353, 919–921. http:/doi.org/10.1038/nphys3711.

Nouzé, H., Henry, P., Noble, M., Martin, V., & Pascal, G. (2004). Large gas hydrate accumulations on the eastern Nankai Trough inferred from new high‐resolution

2‐D seismic data. *Geophysical Research Letters*, *31*, L13308. http://doi.org/10.1029/2004GL019848

Ohde, A., Otsuka, H., Kioka, A., & Ashi, J. (2018). Distribution and depth of bottom-simulating reflectors in the Nankai subduction margin. *Earth, Planets and Space*, *70*, 1–20. http://doi.org/10.1186/s40623-018-0833-5

Saito, M. (1988). DISPER80: a subroutine package for the calculation of seismic normal-mode solutions, in Seismological Algorithms -computational methods and computer programs, p. 469, ed. Doornbos D.J., Academic Press, London, 293–319.

Shinohara, M., Hirata, N., & Takahashi, N. (1994). High resolution velocity analysis of ocean bottom seismometer data by the τ-p method. *Marine Geophysical Research*, *16*, 185–199.

Sladen, A., Rivet, D., Ampuero, J. P., De Barros, L., Hello, Y., Calbris, G., & Lamare, P. (2019). Distributed sensing of earthquakes and ocean-solid Earth interactions on seafloor telecom cables. *Nature Communications*, *10*, 5777. http://doi.org/10.1038/s41467-019-13793-z

Spica, Z. J., Nishida, K., Akuhara, T., Pétrélis, F., Shinohara, M., & Yamada, T. (2020). Marine Sediment Characterized by Ocean-Bottom Fiber-Optic Seismology. *Geophysical Research Letters*, *47*, e2020GL088360. http://doi.org/10.1029/2020GL088360

Stoffa, P. L., Buhl, P., Diebold, J. B., & Wenzel, F. (1981). Direct mapping of seismic data to the domain of intercept time and ray parameter—A plane-wave decomposition. *Geophysics*, *46*(3), 255–267. http://doi.org/10.1190/1.1441197

Tonegawa, T., Araki, E., Kimura, T., Nakamura, T., Nakano, M., & Suzuki, K. (2017). Sporadic low-velocity volumes spatially correlate with shallow very low frequency earthquake clusters. *Nature Communications*, *8*(1), 2048. http://doi.org/10.1038/s41467-017-02276-8

Tonegawa, T., Kimura, T., & Araki, E. (2021). Near-Field Body-Wave Extraction From Ambient Seafloor Noise in the Nankai Subduction Zone. *Frontiers in Earth Science*, *8*, 1–12. http://doi.org/10.3389/feart.2020.610993

Waite, W. F., Helgerud, M. B., Nur A., Pinkston, J. Stern, L. A., Kirby, S. H., Durham, W. B., Holder, G. D., Bishnoi, P. R. (2000). First laboratory measurements of compressional and shear wave speeds through pure methane hydrate at in situ conditions, *Gas Hydrates: Challenges for the Future Blackwell Publishing*, Malden, MA, 912, 1003–1010.

Williams, E. F., Fernández-Ruiz, M. R., Magalhaes, R., Vanthillo, R., Zhan, Z., González-Herráez, M., & Martins, H. F. (2019). Distributed sensing of microseisms and teleseisms with submarine dark fibers. *Nature Communications*, *10*, 5778. http://doi.org/10.1038/s41467-019-13262-7

Wilson, D., & Richards, A. (2005). Seismic imaging of the crust and upper mantle using regularized joint receiver functions, frequency–wave number filtering, and multimode Kirchhoff migration. *Journal of Geophysical Research*, *110*, B05305. http://doi.org/10.1029/2004JB003430

Yamano, M., Uyeda, S., Aoki, Y., & Shipley T. H. (1982). Estimates of heat flow derived from gas hydrates. Geology, 10, 339–343.

Yu, C., Zhan, Z., Lindsey, N. J., Ajo-Franklin, J. B., & Robertson, M. (2019). The Potential of DAS in Teleseismic Studies: Insights From the Goldstone Experiment. *Geophysical Research Letters*, *46*, 1320–1328. http://doi.org/10.1029/2018GL081195

Figure 1. Geometry of the Muroto cable on the seafloor. (a) Black and red lines show the location of the Muroto cable and the section used for the DAS measurements with 10 km increments (yellow circles), respectively. (b) Water depths along the Muroto cable.

Figure 2. Cross-correlation functions (CCFs) s in the time-distance and *f-k* domains for subarray 16 (cable reference point D = 40.7 km) on January 27, 2020. (a) CCFs at 0.4–0.8 Hz aligned as a function of the separation distance between two stations. The two lines show the reference propagation velocities of 1.0 and 2.5 km/s. (b) CCFs in the *f-k* domain. (c) CCFs in the *f-k* domain after applying the Eq. (1) filter to those in Fig. 2b. (d) CCFs in the time-distance domain with the *f-k* filter of Eq. (1).

Figure 3. Slant stacking results of the CCFs at 0.4–0.8 Hz for subarrays (left) 10 and (right) 16 on January 27. 2020. Black and light-blue lines indicate the τ-p data and $\pm 1\sigma$ from the bootstrapping technique with 50 times.

Figure 4. Seismic velocity profiles along the Muroto cable. (a) *Vs* profile along the cable, created using the CCFs on January 29, 2020. Specific features (1)–(4) are observed (see detailed in the text). (b) *Vp* profile along the cable, generated using the CCFs on January 27, 2020. (c) Error for panel (a). (d) Error for panel (b).